

Optically controlled dielectric metasurfaces for dynamic dual-mode modulation on terahertz waves

Haoyang Zhou,[†] Sheng Zhang,[†] Shunjia Wang,^{Ⓧ,†} Yao Yao, Qingnan Cai, Jing Lin, Xiaoying Zheng, Zhuo Wang, Zhensheng Tao,^{*} Qiong He,^{Ⓧ,*} and Lei Zhou^{*}

Fudan University, Key Laboratory of Micro and Nano Photonic Structures (Ministry of Education) and Department of Physics, State Key Laboratory of Surface Physics, Shanghai, China

Abstract. Dynamically controlling terahertz (THz) waves with an ultracompact device is highly desired, but previously realized tunable devices are bulky in size and/or exhibit limited light-tuning functionalities. Here, we experimentally demonstrate dynamic modulation on THz waves with a dielectric metasurface in mode-selective or mode-unselective manners through pumping the system at different optical wavelengths. Quasi-normal-mode theory reveals that the physics is governed by the spatial overlap between wave functions of resonant modes and regions inside resonators perturbed by pump laser excitation at different wavelengths. We further design/fabricate a dielectric metasurface and experimentally demonstrate that it can dynamically control the polarization state of incident THz waves, dictated by the strength and wavelength of the pumping light. We finally numerically demonstrate pump wavelength-controlled optical information encryption based on a carefully designed dielectric metasurface. Our studies reveal that pump light wavelength can be a new external knob to dynamically control THz waves, which may inspire many tunable metadevices with diversified functionalities.

Keywords: dynamic metasurfaces; terahertz; quasi-normal-mode theory; optical pumping.

Received Dec. 15, 2022; revised manuscript received Feb. 14, 2023; accepted for publication Mar. 14, 2023; published online Apr. 8, 2023.

© The Authors. Published by SPIE and CLP under a Creative Commons Attribution 4.0 International License. Distribution or reproduction of this work in whole or in part requires full attribution of the original publication, including its DOI.

[DOI: [10.1117/1.AP.5.2.026005](https://doi.org/10.1117/1.AP.5.2.026005)]

1 Introduction

Dynamic control over terahertz (THz) waves at will with an ultracompact device is important for THz technologies (e.g., biomedical imaging, telecommunications, detection). However, tunable THz devices made of conventional materials are usually of bulky sizes, and limited modulation depths and functionalities, due to weak interactions between naturally existing materials and THz waves.

Metasurfaces, ultrathin metamaterials constructed by planar microstructures exhibiting tailored electromagnetic responses, provide a powerful platform to manipulate light at the deep-subwavelength scale.^{1–7} Combining passive metasurfaces with

different external-stimuli-controlled materials (e.g., semiconductors,^{8–11} 2D materials,^{12–15} phase-change materials,^{16–21} PIN diodes,²² elastic materials,²³ microfluidic materials,²⁴ mechanical devices,^{25,26} and liquid crystals^{27–30}), many tunable metadevices were successfully constructed, which can dynamically control THz waves by applying different external stimuli.³¹ Among these attempts, optically controlled metadevices^{32–35} have gained intensive attention due to their attractive properties, including ultrafast modulation speed and high modulation pixel resolution. In reviewing these efforts, we find that optically controlled metadevices realized so far can be generally categorized into two classes—one enabling frequency-selective light modulation, which is desired in applications such as lasing, sensing, and structural color generations,^{36–39} and the other enabling frequency-unselective light modulation, which is favored in applications such as energy harvesting.^{40,41} In addition, it is highly desired for applications in integrated optics to realize distinct

*Address all correspondence to Zhensheng Tao, zhenshengtao@fudan.edu.cn; Qiong He, qionghe@fudan.edu.cn; Lei Zhou, phzhou@fudan.edu.cn

[†]These authors contributed equally to this work.

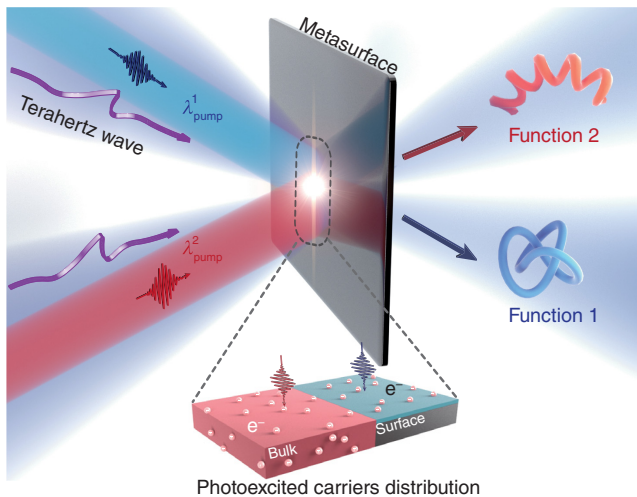


Fig. 1 Schematic of the dynamic dual-mode modulation with an optically controlled dielectric metasurface. Under pumping by external light at different wavelengths, a predesigned dielectric metasurface can exhibit distinct functionalities to manipulate THz waves.

tunable light manipulation upon changing an external knob in a simple device. Several approaches based on metasurfaces have been proposed to achieve distinct light modulations by applying different external knobs.^{42–48} However, some of these achieved metadevices were of relative complicated configurations of meta-atom design to embed different switches. A simple device that can exhibit different types of light responses is still lacking and is in demand for different applications.

In this paper, we propose that the wavelength of pumping light can be an additional knob to achieve dynamic dual-mode modulation on THz waves (see Fig. 1). Specifically, we experimentally demonstrate that a predesigned dielectric metasurface can achieve mode-selective or mode-unselective modulations on incident THz waves, as it is excited by ultrashort pulses at two different wavelengths (e.g., 515 or 1030 nm). Analyses based on quasi-normal-mode (QNM) theory reveal that the underlying physics is determined by the spatial overlap between wave functions of resonant modes and regions perturbed by the pump laser excitation at different wavelengths. Inspired by the discovered mechanism, we demonstrate two active metadevices with distinct light-modulation functionalities in experiments and simulations, respectively. The first device can dynamically change the polarization state of incident THz waves dictated by both pump wavelength and pump fluence, whereas the second one can encrypt optical information and only displays the predesigned holographic pattern when excited by a pump beam at the correct wavelength.

2 Results and Discussion

2.1 Dynamic Dual-mode Modulation: Experiments and Simulations

We start from experimentally demonstrating the dynamic dual-mode modulations on THz waves based on an all-dielectric metasurface. As schematically shown in Fig. 2(a), our metasurface consists of 165 μm high silicon pillars with a cross section of 76.5 $\mu\text{m} \times 206 \mu\text{m}$ arranged in a square lattice with

a periodicity of 275 μm , deposited on a 145 μm thick quartz substrate. Figure 2(b) depicts the scanning electron microscopy (SEM) image of our fabricated sample (see more fabrication details in Section 1 in the [Supplementary Material](#)). We employ homemade optical-pump terahertz-probe spectroscopy⁴⁹ to characterize the laser-excited transmission properties of the sample in THz spectral range (see Section 2 in the [Supplementary Material](#) for more measurement details⁵⁰). The pump laser wavelength λ_{pump} can be adjusted between 515 and 1030 nm. In Figs. 2(c) and 2(d), we compare the THz transmission spectra of the metasurface under excitations of laser beams with different wavelengths and fluences. Here, the time delay is fixed to be $\tau_d = 50$ ps (see Section 2 in the [Supplementary Material](#) for determination of τ_d).

In our experiments, both pump light and probe light are normally incident on the sample and are of linear polarizations with $\mathbf{E} \parallel x$. Without external pumping [top panel of Fig. 2(c)], our metasurface exhibits two resonant modes at $f_1 = 0.675$ THz and $f_2 = 0.714$ THz, respectively, manifested as two clear dips in the measured transmission spectrum. Open circles in Fig. 2(c) represent the measured THz transmission-amplitude spectra of our sample, under the pumping of external light at 515 nm with different optical fluence. As we increase the pump light fluence, we find that while the high-frequency resonant mode (labeled as “Mode 2”) undergoes a clear blueshift in frequency and a resonant strength diminishment, the low-frequency mode (labeled as “Mode 1”) is quite insensitive to the change of optical fluence (see Section 3 in the [Supplementary Material](#) for additional measured results under different excitations). Clearly, mode-selective dynamic modulation is achieved with the metadvice pumped by external light at 515 nm. In stark contrast, when the metasurface is excited by pump light with $\lambda_{\text{pump}} = 1030$ nm, the two resonant modes are modulated strongly and simultaneously, manifested by both the resonant-frequency blueshifts and the mode-strength diminishments [see Fig. 2(d)]. In fact, increasing the pump fluence to 40 $\mu\text{J}/\text{cm}^2$ can completely “kill” two resonant modes, as shown in the transmission-amplitude spectra and transmission-phase spectra (see Fig. S6 in Section 3 in the [Supplementary Material](#)). Obviously, mode-unselective dynamic modulation is achieved with our metadvice as pumped by external light at 1030 nm.

We perform finite-difference time-domain (FDTD) simulations to calculate the transmission spectra of our metasurface under different photoexcitations. Optically pumping silicon at frequencies above its bandgap can induce free carriers in its conduction band, thus modulating the permittivity of silicon. Under different pump fluence, permittivity of silicon can be well described by the Drude model,⁵¹

$$\tilde{\epsilon}^{(p)}(F) = \epsilon^{(0)} - \frac{[N_e(F) + N_0]e^2}{m_{\text{eff}}\epsilon_0(\omega^2 + i\omega\gamma_D)}, \quad (1)$$

where $\epsilon^{(0)} = 11.9025$ denotes the static permittivity of silicon, $N_0 = 5 \times 10^9 \text{ cm}^{-3}$ is the static carrier density of intrinsic silicon (estimated at temperature 296 K), N_e denotes the excited carrier density, which depends on the optical absorbed pumping fluence F through a formula established in a prior work,⁵² $m_{\text{eff}} = 0.16m_e$ is the effective mass of the carrier (m_e is the free electron mass⁵³), and $\gamma_D = 1 \times 10^{13}$ Hz is the damping rate (determined by carrier–phonon collisions at low carrier densities⁵⁴). We note that the optically excited carriers are only distributed in the region of silicon where pump light can penetrate inside.

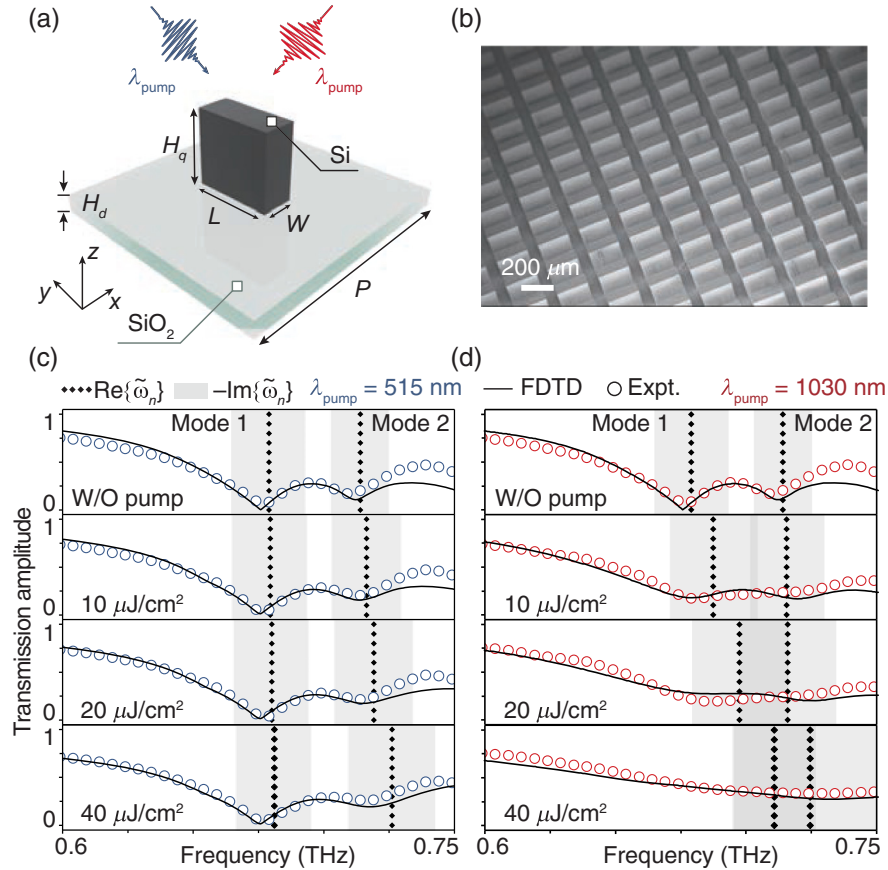


Fig. 2 Experimental demonstration of the dynamic dual-mode THz wave modulation. (a) Schematic of the basic meta-atom consisting of a quartz substrate and silicon pillar with the following geometrical parameters: $H_q = 165$, $W = 76.5$, $L = 206$, $H_d = 145$, $P = 275$, all in units of μm . (b) Tilt-view SEM image of the fabricated sample. (c), (d) Measured (open circles) and simulated (solid lines) transmission amplitude spectra of the fabricated metasurface, under external pumping at (c) 515 nm and (d) 1030 nm with different pump fluences. Black dotted vertical lines and gray shaded areas denote the real part and negative imaginary part of $\tilde{\omega}_n$ calculated by the QNM theory in different cases.

The thickness δ of such an “excited” layer is inversely proportional to the absorption coefficient α at different pump wavelengths, which can be retrieved from the refractive index of silicon.⁵⁵ Figure 3(a) depicts how δ varies against the pump light wavelength λ_{pump} , which determines the regions in our silicon pillars where the permittivity of silicon should be replaced by Eq. (1). Although $\delta_{515} = 1.05 \mu\text{m}$ is much smaller than the height of silicon pillar ($H_q = 165 \mu\text{m}$), indicating that the 515-nm pump light can only affect a thin layer on top of the silicon pillar, the 1030-nm pump light can penetrate inside the whole silicon pillar ($\delta_{1030} = 341 \mu\text{m} > H_q$), as shown in the insets of Fig. 3(a). Putting this information into FDTD simulations, the tunable THz responses of our proposed metasurfaces induced by different optical pumping can be well described. And then, we compute the transmission spectra of the metadvice under different pump conditions (e.g., pump light wavelength and fluence). FDTD-simulated spectra are shown in Figs. 2(c) and 2(d) as solid lines, which have captured all salient features of experimental results well (see Section 4 in the [Supplementary Material](#) for more simulation details).

2.2 Mechanism Analyses

We now reveal the underlying physics with the help of QNM theory.⁵⁶ Quasi-normal modes are resonant modes supported by an open system, and their eigen frequencies are generally complex values with imaginary parts characterizing the damping rates of the modes due to absorption and/or radiation. We first employ the QNM theory to compute the complex eigen frequencies of two resonant modes supported by our dielectric metasurface under different photoexcitation conditions (see Section 5 in the [Supplementary Material](#) for details of our QNM calculations). Without external pumping, we get $\{\tilde{\omega}_1^{(0)}/2\pi = 0.679 - 0.028i; \tilde{\omega}_2^{(0)}/2\pi = 0.714 - 0.022i\}$, all in the units of THz. Obtaining the eigen frequencies $\tilde{\omega}_n^{(p)}$ of the photoexcited system with the QNM theory, we then compute the eigen frequency shifts using $\Delta\tilde{\omega}_n = \tilde{\omega}_n^{(p)} - \tilde{\omega}_n^{(0)}$, and depict the values of $-\text{Im}(\Delta\tilde{\omega}_n)$ as open triangles and open stars in Figs. 3(c) and 3(d), respectively, for different pump wavelengths with varying photoexcitation fluences F . We find that the $-\text{Im}(\Delta\tilde{\omega}_n) \sim F$ relations exhibit distinct behaviors in two cases. In the case of

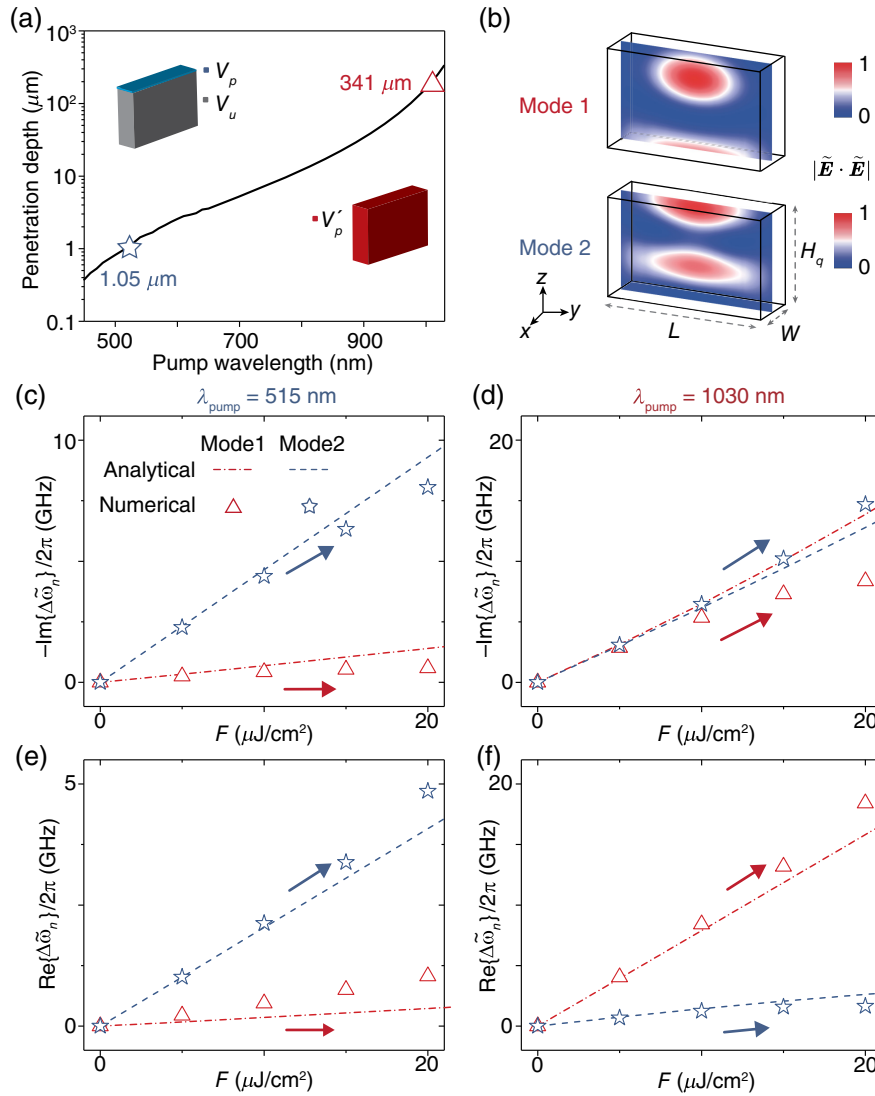


Fig. 3 Working mechanism of the dynamic dual-mode modulation. (a) The solid line represents the calculated penetration depth of silicon versus the wavelength; the blue star and red triangle represent the penetration depths of silicon for pump light at 515 and 1030 nm, respectively; the left (right) inset depicts the perturbed region [highlighted by red (blue) color] inside the silicon pillar pumped by external light at 515 nm (1030 nm). (b) FEM-simulated normalized spatial distributions of $|\tilde{\mathbf{E}} \cdot \tilde{\mathbf{E}}|$ at eigen frequencies of Modes 1 and 2 inside the silicon resonator. (c)–(f) Numerically simulated and analytically calculated values of (c), (d) $-\text{Im}(\Delta\tilde{\omega}_n)$ and (e), (f) $\text{Re}(\Delta\tilde{\omega}_n)$ for two resonant modes as varying optical fluence F of pump light at the wavelength of (c), (e) 515 nm and (d), (f) 1030 nm, respectively.

$\lambda_{\text{pump}} = 515 \text{ nm}$, only $-\text{Im}(\Delta\tilde{\omega}_n)$ of Mode 2 is strongly modulated by F , while that of Mode 1 is hardly affected by photoexcitation. In the case of $\lambda_{\text{pump}} = 1030 \text{ nm}$, however, $-\text{Im}(\Delta\tilde{\omega}_n)$ of both modes are simultaneously modulated by F dramatically. The $\text{Re}(\Delta\tilde{\omega}_n) \sim F$ relations depicted in Figs. 3(e) and 3(f) exhibit similar behaviors to those of $-\text{Im}(\Delta\tilde{\omega}_n)$, i.e., only Mode 2 is modulated in the case of $\lambda_{\text{pump}} = 515 \text{ nm}$, but two modes are simultaneously modulated in the case of $\lambda_{\text{pump}} = 1030 \text{ nm}$. We use dashed lines and shaded regions to represent the numerically computed $\text{Re}(\tilde{\omega}_n^{(p)})$ and $-\text{Im}(\tilde{\omega}_n^{(p)})$ in the transmission spectra shown in Figs. 2(c) and 2(d) for different excitation conditions, respectively. We find that the

QNM computed values of $\Delta\tilde{\omega}_n$ are in nice agreement with the measured/simulated spectra and have well explained the evolutions of two resonant modes at two pump wavelengths discovered experimentally and numerically [see Figs. 2(c) and 2(d)]. Meanwhile, the discrepancy between FDTD-simulated and QNM-computed results was due to the low Q resonant modes of the meta-atom design.

Now that the QNM-computed results have captured all salient features of the simulated and measured results well, we explore the underlying physics based on the QNM theory. Under weak photoexcitation, the shift of complex eigen frequency due to photoexcitation can be calculated by the standard perturbation theory within the QNM framework,^{57,58}

$$\begin{aligned}\Delta\tilde{\omega}_n &= -\tilde{\omega}_n^{(0)} \cdot \iiint \Delta\tilde{\epsilon}(\vec{\mathbf{r}}) \tilde{\mathbf{E}}_n^{(p)}(\vec{\mathbf{r}}) \cdot \tilde{\mathbf{E}}_n^{(0)}(\vec{\mathbf{r}}) d\vec{\mathbf{r}} \\ &= -\tilde{\omega}_n^{(0)} \cdot \Delta\tilde{\epsilon} \cdot \iiint_{\vec{\mathbf{r}} \in \text{PR}} \tilde{\mathbf{E}}_n^{(p)}(\vec{\mathbf{r}}) \cdot \tilde{\mathbf{E}}_n^{(0)}(\vec{\mathbf{r}}) d\vec{\mathbf{r}}.\end{aligned}\quad (2)$$

Here, $\tilde{\mathbf{E}}_n^{(p)}(\vec{\mathbf{r}})$ represents the perturbed eigen wave function derived from the unperturbed eigen wave function $\tilde{\mathbf{E}}_n^{(0)}(\vec{\mathbf{r}})$ in the QNM theory, and $\Delta\tilde{\epsilon}(\vec{\mathbf{r}}) = \epsilon_0[\tilde{\epsilon}^{(p)}(\vec{\mathbf{r}}) - \epsilon^{(0)}(\vec{\mathbf{r}})]$ denotes the permittivity change in our system due to photoexcitation, being nonzero [$\Delta\tilde{\epsilon}(\vec{\mathbf{r}}) = \Delta\tilde{\epsilon}$] only inside the perturbed region (PR), which is a layer with thickness δ sensitively depending on the pump wavelength λ_{pump} [see Fig. 3(a)]. Detailed discussions on Eq. (2) can be found in Section 5 in the [Supplementary Material](#). As shown in Figs. 3(c) and 3(d), complex frequency shifts of two resonant modes (dotted dashed lines and dashed lines) calculated by Eq. (2) are in nice agreement with those obtained with the QNM-calculated results (open triangles and open stars) under different pumping conditions, especially in weak-excitation cases where the perturbation theory is better applicable.

Equation (2) provides an analytical platform to understand the intrinsic physics. As shown in the insets of Fig. 3(a), the perturbed region is a thin layer on top of the pillar at pump wavelength 515 nm, but becomes the whole pillar at 1030 nm. Meanwhile, eigen wave functions of the two modes also exhibit distinct spatial distributions. As shown in Fig. 3(b), while Mode 1 is a dipole resonant mode with \mathbf{E} -field mainly distributing inside the central region of the resonator (with slight asymmetry induced by the substrate), Mode 2 is a quadrupole mode with the \mathbf{E} -field mainly localized on the resonator surface. The distinct features of the perturbed regions and eigen wave functions can help us understand the physics underlying the discovered phenomena. Since pump light at 515 nm can only perturb the surface region of our silicon pillar, we immediately understand that only Mode 2 can be strongly modulated by external pumping, since this mode has a strong \mathbf{E} -field on the pillar surface. In contrast, Mode 1 is hardly affected by external pumping, since it does not have a strong \mathbf{E} -field on the surface. Meanwhile, in the case of 1030 nm pumping, the perturbed region covers the entire silicon pillar, which explains why both modes are simultaneously modulated by external pumping.

The analytical formula [Eq. (2)] can also help us understand an intriguing effect displayed in Figs. 2(c)–2(f), i.e., the two $\text{Re}(\Delta\tilde{\omega}_n) \sim F$ relations exhibit different variation slopes as compared to their corresponding $-\text{Im}(\Delta\tilde{\omega}_n) \sim F$ curves in the case of $\lambda_{\text{pump}} = 1030$ nm. The underlying physics is that, in the case of $\lambda_{\text{pump}} = 1030$ nm, field integrations $\iiint_{\vec{\mathbf{r}} \in \text{PR}} \tilde{\mathbf{E}}_n^{(p)}(\vec{\mathbf{r}}) \cdot \tilde{\mathbf{E}}_n^{(0)}(\vec{\mathbf{r}}) d\vec{\mathbf{r}}$ of two resonant modes exhibit distinct phases so that their contributions to $\text{Re}(\Delta\tilde{\omega}_n)$ and $\text{Im}(\Delta\tilde{\omega}_n)$ can be quite different, although both $\text{Re}(\Delta\tilde{\omega}_n)$ and $\text{Im}(\Delta\tilde{\omega}_n)$ are strongly modulated by external pumping. Detailed discussions can be found in Section 5 in the [Supplementary Material](#).

Before ending this section, it is worth emphasizing that our dual-mode modulation originates from the spatial permittivity modification induced by different optical pumping with different wavelengths, which is totally different from recent works of pump light wavelength-dependent tunable metasurfaces based on a wavelength-dependent absorption feature⁵⁹ or multitype materials-induced different time responses.⁴⁶ In addition, our proposed modulation scheme does not depend on the linewidth or the spectral position of resonant modes, and it is applicable to

other frequency regimes with appropriate material systems. For example, in mid-infrared or near-infrared regimes, one can use the GaAs⁶⁰ or GaN⁶¹ to construct dielectric metasurfaces to achieve similar device functionalities, respectively (see Section 6 in the [Supplementary Material](#) for appropriate materials and their working frequency regime).

2.3 Applications

Having revealed the underlying physics of the dynamic dual-mode modulation, we now employ the discovered strategy to realize two metadevices with different functionalities in experiments and numerical calculations, respectively.

2.3.1 Dynamic dual-mode metapolarizer

We first experimentally realize a tunable metadvice that can dynamically manipulate the polarization of THz wave depending on external photoexcitation. The designed metadvice is of the same configuration as that shown in Fig. 2(a), but with different geometric parameters: $W = 74.5$, $L = 168$, $H_d = 175$, $H_q = 170$, $P = 285$, all in the units of micrometers. Due to the rectangular shape of the meta-atom, the designed metasurface exhibits distinct transmission spectrum for x - and y -polarized incident THz waves, and such anisotropic responses can be dynamically modulated by external pumping. As a result, the designed metadvice can dynamically control the polarization state of the impinging THz wave, dictated by the wavelength and fluence of the pump light [Fig. 4(a)].

We fabricate out a sample according to the design [see inset of Fig. 4(a) for its top-view SEM picture], and then experimentally characterize its transmission properties under different photoexcitation. Orange open stars and red open circles in Fig. 4(d) depict the measured spectra of transmission amplitude $|t_{xx}|$ and $|t_{yy}|$, respectively, and blue diamonds represent the measured spectrum of phase difference $\Delta\Phi = \Phi_{xx} - \Phi_{yy}$, for our metadvice without any photoexcitation (see Section 7 in the [Supplementary Material](#) for more experimental and simulated results). We find two clear resonant dips at 0.704 and 0.738 THz in the $|t_{xx}|$ spectrum, which exhibit similar field patterns to the two modes studied in last section (see Section 8 in the [Supplementary Material](#) for discussions at a frequency near Mode 2). Meanwhile, a broadband dip is found in the $|t_{yy}|$ spectrum around 0.66 THz, which contains two high-order modes coupled together (see Section 9 in the [Supplementary Material](#) for more discussions). Choosing the working frequency as 0.695 THz [denoted by a gray dashed line in Fig. 4(d)], we find $|t_{xx}| = |t_{yy}| = 0.25$ and $\Delta\Phi = \pi$, indicating that the metasurface behaves as a half wave plate at this frequency. We retrieve the polarization pattern of the THz wave transmitted through our device under the illumination of normally left circularly polarized (LCP) beam at 0.695 THz and depict the obtained pattern using the black star in Fig. 4(c) labeled as “W/O pump.” The polarization pattern is nearly a right circularly polarized (RCP) state with ellipticity angle of 43 deg and azimuthal angle of -44 deg, as expected.

We now study how the transmission characteristics (and thus the polarization manipulation capability) of our metadvice vary under different photoexcitations. Clearly, transmission coefficient t_{xx} (with both amplitude and phase) at the working frequency is mainly affected by the x -polarized mode at 0.704 THz. As discussed in the last section, such a mode is a dipole resonant mode, which is drastically modulated by

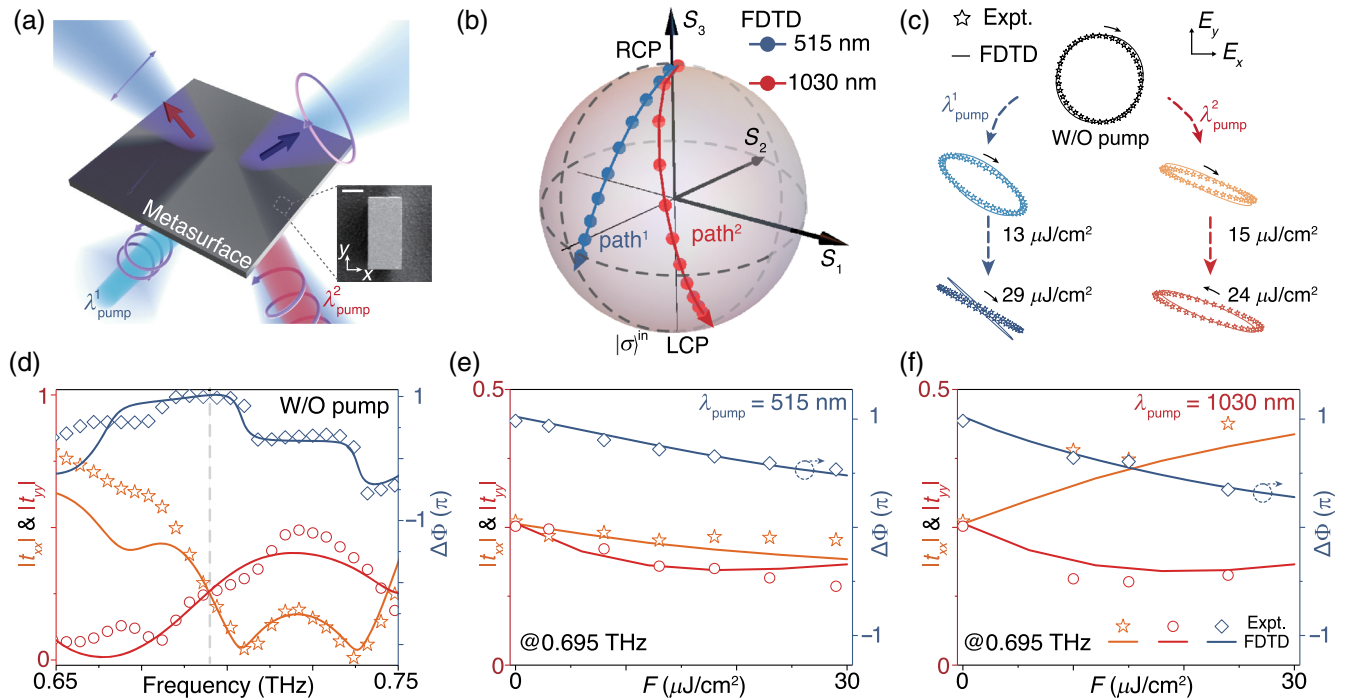


Fig. 4 Experimental demonstration of a dynamic dual-mode metapolarizer. (a) Schematic of the metapolarizer exhibiting different polarization-manipulation functionality as pumped by external light at different wavelengths. The inset depicts part of the SEM image of the fabricated sample with a scale bar (white line) of 50 μm . (b) FDTD-simulated polarization trajectories on Poincaré's sphere of THz waves at 0.695 THz passing through the metadvice pumped by external light at different wavelengths with varying pump fluences. (c) Measured (stars) and simulated (line) polarization states of THz waves at 0.695 THz transmitted through the metadvice under the photoexcitation of 515-nm (blue) and 1030-nm (red) pump light with different pump fluences. (d) Measured and simulated spectra of transmission amplitudes ($|t_{xx}|$ and $|t_{yy}|$) and cross-polarization phase difference ($\Delta\Phi$) of the metadvice without photoexcitation. (e), (f) Measured and simulated evolutions of transmission amplitude and cross-polarization phase difference $\Delta\Phi$ of the metadvice at 0.695 THz as a function of pump fluence under photoexcitation at the wavelength of (e) 515 nm and (f) 1030 nm, respectively.

external pumping at 1030 nm but is hardly affected by external pumping at 515 nm. It is thus not surprising to see that our measured $|t_{xx}|$ at 0.695 THz increases substantially as the pump fluence F varies at 1030 nm [orange star in Fig. 4(f)], but remains relatively stable as the pump wavelength changes to 515 nm [see orange open circles in Fig. 4(e)]. Meanwhile, we find t_{yy} at 0.695 THz is influenced by two high-order y -polarized modes at frequencies below 0.695 THz (see Section 9 in the [Supplementary Material](#) for more discussions), and thus the modulation of $|t_{yy}|$ is quite moderate and does not exhibit obvious difference for two pump light wavelengths [see red open circles in Figs. 4(e) and 4(f)]. Finally, the measured cross-polarization phase difference $\Delta\Phi$ decreases as F increases in both cases, since pumping the system essentially diminishes all resonances, and such a trend is more dramatic in the case of 1030-nm light pumping [see blue diamonds in Fig. 4(f)].

We can easily retrieve the polarization-control functionality of our device at 0.695 THz through the measured pump fluence-dependent transmission characteristics. Under the pumping at 515 nm, as F increases, we find that $\Delta\Phi$ gradually decreases from π to $\pi/2$ with $|t_{xx}| \approx |t_{yy}|$ kept approximately, indicating that our device changes its functionality from a half-wave plate to a quarter-wave plate. Such a trend has been well confirmed by

the retrieved polarization patterns of THz waves transmitted through the metadvice pumped by 515-nm light with fluences 13 and 29 $\mu\text{J}/\text{cm}^2$ [see Fig. 4(c)], respectively. Indeed, the output polarization state evolves from RCP to linear polarization (LP) with \mathbf{E} -field lying at an angle of -43 deg with respect to the x axis as pump fluence increases. The functionality of our metadvice changes as the pump light wavelength is switched to 1030 nm. In this case, the ellipticity of THz wave transmitted through the device changes from 43 deg (nearly RCP) to 0 deg (LP) and further to -14 deg (left-handed elliptically polarized) as the pump fluence increases from 0 to 15 $\mu\text{J}/\text{cm}^2$ and to 30 $\mu\text{J}/\text{cm}^2$ [see Fig. 4(f)]. Meanwhile, compared to the 515-nm pump case, the azimuthal angle of the transmitted THz wave is changed to -20 deg [see Fig. 4(c)]. These differences are caused by distinct F -dependent amplitude ratio $|t_{yy}|/|t_{xx}|$ and phase-difference $\Delta\Phi$ in the 1030-nm pump case compared with the 515-nm pump case.

FDTD simulations are in nice agreement with the measured transmission spectra and pump fluence-dependent transmission characteristics [see solid lines in Figs. 4(d) and 4(f)]. In addition, we can retrieve from the FDTD results the polarization states of THz waves transmitted through the device, and plot their trajectories on Poincaré's sphere as two dotted solid lines for two

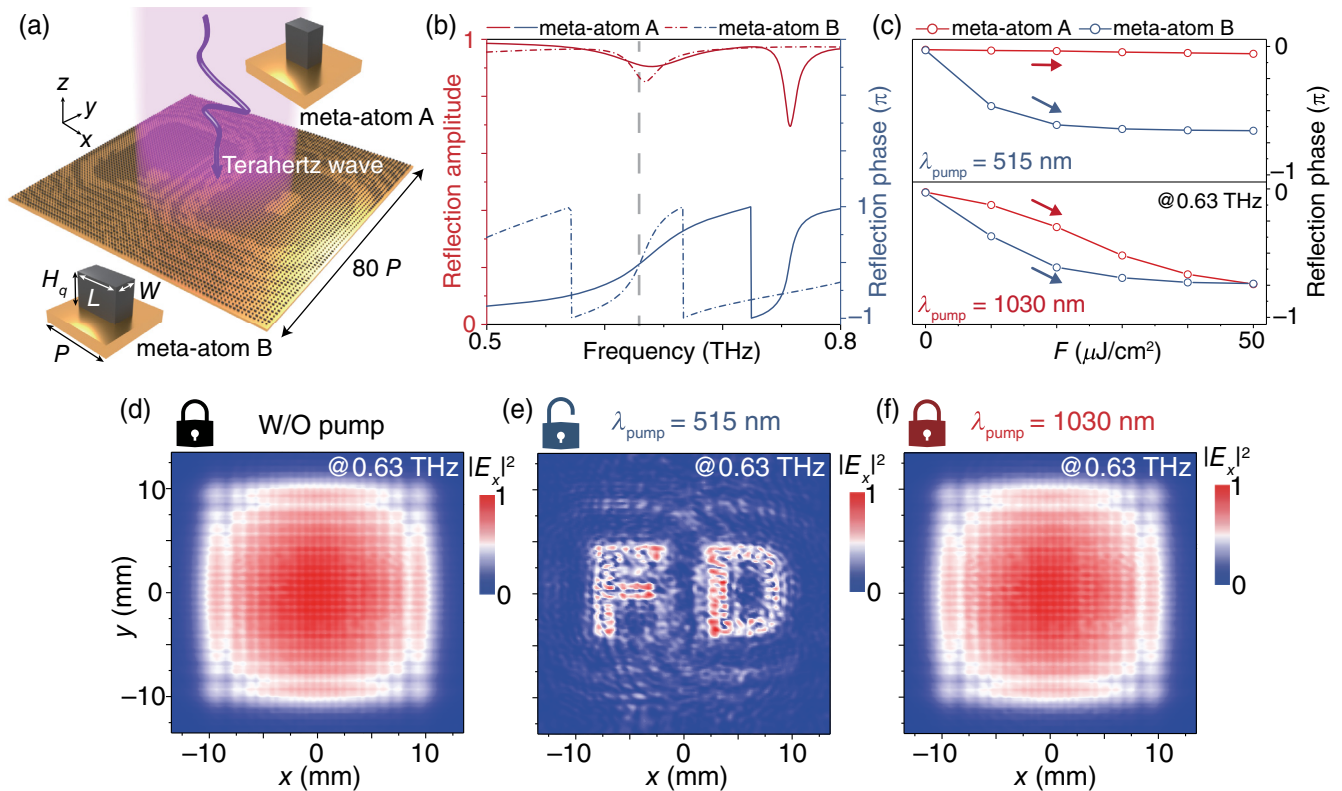


Fig. 5 Numerical demonstration of an optical information encryption metasurface. (a) Schematic of the proposed metadvice composed of two basic meta-atoms (see insets) arranged in a pre-designed sequence. Geometrical parameters of meta-atom A are set as $P = 288$, $H_q = 130$, $L = 102$, $W = 70$, all in units of micrometers, while the length and width of meta-atom B are adjusted to $170 \mu\text{m}$ and $86 \mu\text{m}$, respectively. (b) FDTD-simulated spectra of reflection amplitude and phase of two periodic metasurfaces consisting of arrays of meta-atom A (red and blue solid lines) and meta-atom B (red and blue dotted dashed lines), respectively. Gray dashed line denotes the working frequency 0.63 THz. (c) Reflection phases of two meta-atoms under different pump fluences at different wavelengths, obtained by FDTD simulations at 0.63 THz. (d)–(f) Computed normalized field distributions on the plane at $z = 25\lambda$ above the metasurface shone by normally incident THz wave at 0.63 THz, under different pumping conditions (d) without any photoexcitation, (e) pumped by 515-nm light with fluence $50 \mu\text{J}/\text{cm}^2$, and (f) pumped by 1030-nm light with fluence $50 \mu\text{J}/\text{cm}^2$.

pump wavelengths [see Fig. 4(b)]. From Figs. 4(b) and 4(c), we find that both increasing the pump fluence and changing the pump wavelength can modulate the polarization state of the transmitted THz wave dramatically, offering our metadvice expanded polarization-control capabilities. Here, we note that the experimentally achieved dynamic range of polarization modulation is mainly determined by the limited tunable range on transmission amplitude and phase for the x -polarized THz beam. Actually, to expand the dual-mode polarization controllability, one can use the reflection-type metasurfaces, which can provide larger tuning range in terms of reflection amplitude and phase, as shown in Section 10 in the [Supplementary Material](#).

2.3.2 Optical information encryption

The newly discovered strategy can also enable the application for optical information encryption. Figure 5(a) schematically depicts the proposed metadvice. Different from the metasurfaces discussed in previous sections, here we add a gold (Au)

substrate to the bottom of our structure serving as a reflection mirror. In the spirit of phase hologram, our metasurface consists of two basic meta-atoms arranged in pre-designed sequence [see Fig. 5(a)]. These two meta-atoms (labeled as “A” and “B,” respectively) exhibit distinct geometrical parameters and thus different optical responses. As shown in Fig. 5(b), as illuminated by normally incident x -polarized THz wave, two different meta-atoms exhibit similar reflection amplitudes ($|r_A| = 0.90$, $|r_B| = 0.87$) and phases ($\Phi_A = 0$, $\Phi_B = 0$) at the working frequency 0.63 THz (see dashed line) without photoexcitation. As pumped by external light, resonant modes related to different meta-atoms exhibit distinct pump fluence dependence dictated by the mode wave functions and the pump light wavelength. In particular, in the case of 515-nm light pumping, Φ_A remains nearly unchanged, whereas Φ_B changes dramatically as F increases, while both Φ_A and Φ_B vary simultaneously against F as the pump wavelength is switched to 1030 nm. Thus, at the working frequency, the reflection phase difference between the two meta-atoms $\Phi_A - \Phi_B$ reaches about $-2/3\pi$ as

the meta-atoms are pumped by external light at 515 nm with $F = 50 \mu\text{J}/\text{cm}^2$, whereas $\Phi_A - \Phi_B$ is nearly 0 as the pump light wavelength is switched to 1030 nm, being the same as the unpumped case. We can thus employ two meta-atoms as building blocks to construct a metahologram based on their phase responses at $\lambda_{\text{pump}} = 515 \text{ nm}$ and $F = 50 \mu\text{J}/\text{cm}^2$. Intriguingly, under x -polarized THz illumination at 0.63 THz, while the designed metadvice can exhibit the predesigned hologram image as pumped by 515-nm light with $F = 50 \mu\text{J}/\text{cm}^2$, we expect that the image must be destroyed as the pump wavelength changes to 1030 nm or the pump light is turned off.

We verify the above predictions based on numerical calculations. Based on the phase responses of two meta-atoms at $\lambda_{\text{pump}} = 515 \text{ nm}$ and $F = 50 \mu\text{J}/\text{cm}^2$, we design a metasurface that can exhibit the image of “FD” as shown by the x -polarized THz wave at 0.63 THz. Retrieving the desired phase distribution of the metasurface based on the modified Gerchberg–Saxton algorithm, we then construct the device using 80×80 meta-atoms according to the retrieved phase distribution. We perform analytical calculations based on the dyadic Green’s function method to compute the output holographic images detected on a plane at $z = 25\lambda$ above the metasurface, as it is shown by the x -polarized THz wave at 0.63 THz under different pumping conditions (see more details in Section 11 in the [Supplementary Material](#)). As shown in Figs. 5(d)–5(f), a correct holographic image is displayed only in the case of $\lambda_{\text{pump}} = 515 \text{ nm}$ and $F = 50 \mu\text{J}/\text{cm}^2$ [see Fig. 5(e)], whereas no image is observed as the pump wavelength changes to 1030 nm [Fig. 5(f)] or as the pump light is switched off [Fig. 5(d)]. These results show that correct information can only be released under a particular pumping condition, well suited for information-encryption applications.

3 Conclusions and Discussions

In conclusion, we propose a new strategy to achieve dynamic dual-mode light modulation, and experimentally verify the concept in the THz regime. Specifically, we demonstrate that a specifically designed dielectric metasurface can realize mode-selective or mode-unselective dynamic modulation on THz waves, as pumped by external light at different wavelengths. QNM calculations reveal that the physics is governed by distinct overlapping between resonant wave functions and perturbed regions in resonators under different pumping conditions. Recently, Cong et al.⁶² introduced the temporal loss boundary to temporally engineer the photonic cavity. We expect that the combination of spatial overlap decided by wave function and temporal overlap determined by the Q factor of the resonant mode may lead to a fancier dynamic spatiotemporal modulation. Two metadevices are demonstrated experimentally and numerically, respectively, with the first one being a metapolarizer exhibiting expanded polarization-control capabilities dictated by the strength and wavelength of pump light, and the second one displaying the encrypted holography image as pumped by light with correct wavelength and fluence. Our studies reveal that pump light wavelength can be another degree of freedom to tune the functionality of a dielectric metadvice, which significantly expand our capabilities to dynamically control light waves. The discovered mechanism can inspire many new tunable devices with distinct light-modulation functionalities, being highly desired for applications such as sensing, security, and next-generation wireless communications.

Acknowledgments

This work was supported by the National Key Research and Development Program of China (Grant No. 2022YFA1404700), the National Natural Science Foundation of China (Grant Nos. 12221004, 11734007, and 11874121), and the Natural Science Foundation of Shanghai (Grant Nos. 20JC1414601 and 19JC1410900). L. Z. and Q. H. acknowledge technical support from the Fudan Nanofabrication Laboratory for sample fabrications. H. Z., S. Z., and S. W. contributed equally to this work. All authors contributed to the discussions and preparation of the manuscript.

References

1. N. Yu et al., “Light propagation with phase discontinuities: generalized laws of reflection and refraction,” *Science* **334**(6054), 333–337 (2011).
2. S. Sun et al., “Gradient-index meta-surfaces as a bridge linking propagating waves and surface waves,” *Nat. Mater.* **11**(5), 426–431 (2012).
3. Q. Ma et al., “Information metasurfaces and intelligent metasurfaces,” *Photon. Insights* **1**(1), R01 (2022).
4. A. Arbabi et al., “Dielectric metasurfaces for complete control of phase and polarization with subwavelength spatial resolution and high transmission,” *Nat. Nanotechnol.* **10**(11), 937–943 (2015).
5. S. Sun et al., “High-efficiency broadband anomalous reflection by gradient meta-surfaces,” *Nano Lett.* **12**(12), 6223–6229 (2012).
6. J. Kim et al., “Tunable metasurfaces towards versatile metalenses and metaholograms: a review,” *Adv. Photonics* **4**(02), 024001 (2022).
7. Y. Guo et al., “Classical and generalized geometric phase in electromagnetic metasurfaces,” *Photon. Insights* **1**(1), R03 (2022).
8. J. Gu et al., “Active control of electromagnetically induced transparency analogue in terahertz metamaterials,” *Nat. Commun.* **3**(1), 1151 (2012).
9. L. Cong and R. Singh, “Spatiotemporal dielectric metasurfaces for unidirectional propagation and reconfigurable steering of terahertz beams,” *Adv. Mater.* **32**(28), 2001418 (2020).
10. Y. Yang et al., “Femtosecond optical polarization switching using a cadmium oxide-based perfect absorber,” *Nat. Photonics* **11**(6), 390–395 (2017).
11. P. Wu et al., “Dynamic beam steering with all-dielectric electro-optic III–V multiple-quantum-well metasurfaces,” *Nat. Commun.* **10**(1), 3654 (2019).
12. Z. Miao et al., “Widely tunable terahertz phase modulation with gate-controlled graphene metasurfaces,” *Phys. Rev. X* **5**(4), 041027 (2015).
13. B. Zeng et al., “Hybrid graphene metasurfaces for high-speed mid-infrared light modulation and single-pixel imaging,” *Light Sci. Appl.* **7**(1), 51 (2018).
14. S. Biswas et al., “Broadband electro-optic polarization conversion with atomically thin black phosphorus,” *Science* **374**(6566), 448–453 (2021).
15. Q. Li et al., “Gate-tuned graphene meta-devices for dynamically controlling terahertz wavefronts,” *Nanophotonics* **11**(9), 2085–2096 (2022).
16. Y. Kim et al., “Phase modulation with electrically tunable vanadium dioxide phase-change metasurfaces,” *Nano Lett.* **19**(6), 3961–3968 (2019).
17. S. Abdollahramezani et al., “Dynamic hybrid metasurfaces,” *Nano Lett.* **21**(3), 1238–1245 (2021).
18. B. Chen et al., “Electrically addressable integrated intelligent terahertz metasurface,” *Sci. Adv.* **8**(41), 1296 (2022).
19. S. Zhang et al., “Nonvolatile reconfigurable terahertz wave modulator,” *Photonix* **3**(1), 7 (2022).

20. F. Shu et al., “Electrically driven tunable broadband polarization states via active metasurfaces based on joule-heat-induced phase transition of vanadium dioxide,” *Laser Photonics Rev.* **15**(10), 2100155 (2021).
21. B. Chen et al., “Programmable terahertz metamaterials with non-volatile memory,” *Laser Photonics Rev.* **16**(4), 2100472 (2022).
22. L. Li et al., “Electromagnetic reprogrammable coding-metasurface holograms,” *Nat. Commun.* **8**(1), 197 (2017).
23. S. M. Kamali et al., “Highly tunable elastic dielectric metasurface lenses,” *Laser Photonics Rev.* **10**(6), 1002–1008 (2016).
24. W. Yang et al., “Dynamic bifunctional metasurfaces for holography and color display,” *Adv. Mater.* **33**(36), 2101258 (2021).
25. Q. Xu et al., “Mechanically reprogrammable Pancharatnam–Berry metasurface for microwaves,” *Adv. Photonics* **4**(1), 016002 (2022).
26. X. Cai et al., “Dynamically controlling terahertz wavefronts with cascaded metasurfaces,” *Adv. Photonics* **3**(3), 036003 (2021).
27. A. Komar et al., “Dynamic beam switching by liquid crystal tunable dielectric metasurfaces,” *ACS Photonics* **5**(5), 1742–1748 (2018).
28. I. Kim et al., “Pixelated bifunctional metasurface-driven dynamic vectorial holographic color prints for photonic security platform,” *Nat. Commun.* **12**(1), 3614 (2021).
29. W. Li et al., “Dual-color terahertz spatial light modulator for single-pixel imaging,” *Light Sci. Appl.* **11**(1), 191 (2022).
30. Z. Shen et al., “Liquid crystal integrated metalens with tunable chromatic aberration,” *Adv. Photonics* **2**(3), 036003 (2020).
31. Q. He, S. Sun, and L. Zhou, “Tunable/reconfigurable metasurfaces: physics and applications,” *Research* **2019**, 1849272 (2019).
32. L. Nicholls et al., “Designer photonic dynamics by using non-uniform electron temperature distribution for on-demand all-optical switching times,” *Nat. Commun.* **10**(1), 2967 (2019).
33. K. Fan, I. Shadrivov, and W. Padilla, “Dynamic bound states in the continuum,” *Optica* **6**(2), 169–173 (2019).
34. S. Han et al., “All-dielectric active terahertz photonics driven by bound states in the continuum,” *Adv. Mater.* **31**(37), 1901921 (2019).
35. J. Guo et al., “Reconfigurable terahertz metasurface pure phase holograms,” *Adv. Opt. Mater.* **7**(10), 1801696 (2019).
36. C. de Galarreta et al., “Reconfigurable multilevel control of hybrid all-dielectric phase-change metasurfaces,” *Optica* **7**(5), 476–484 (2020).
37. A. Titl et al., “Imaging-based molecular barcoding with pixelated dielectric metasurfaces,” *Science* **360**(6393), 1105–1109 (2018).
38. B. Yang et al., “Ultrahighly saturated structural colors enhanced by multipolar-modulated metasurfaces,” *Nano Lett.* **19**(7), 4221–4228 (2019).
39. F. Yesilkoy et al., “Ultrasensitive hyperspectral imaging and bio-detection enabled by dielectric metasurfaces,” *Nat. Photonics* **13**(6), 390–396 (2019).
40. H. Lin et al., “A 90-nm-thick graphene metamaterial for strong and extremely broadband absorption of unpolarized light,” *Nat. Photonics* **13**(4), 270–276 (2019).
41. Y. Zhou et al., “Ultra-broadband metamaterial absorbers from long to very long infrared regime,” *Light Sci. Appl.* **10**(1), 138 (2021).
42. M. Manjappa et al., “Reconfigurable MEMS Fano metasurfaces with multiple-input–output states for logic operations at terahertz frequencies,” *Nat. Commun.* **9**(1), 4056 (2018).
43. S. Venkatesh et al., “A high-speed programmable and scalable terahertz holographic metasurface based on tiled CMOS chips,” *Nat. Electron.* **3**(12), 785–793 (2020).
44. K. Sengupta, T. Nagatsuma, and D. M. Mittleman, “Terahertz integrated electronic and hybrid electronic–photonic systems,” *Nat. Electron.* **1**(12), 622–635 (2018).
45. J. Zhang et al., “Electrically tunable metasurface with independent frequency and amplitude modulations,” *ACS Photonics* **7**(1), 265–271 (2020).
46. Y. Hu et al., “Pump-color selective control of ultrafast all-optical switching dynamics in metaphotonic devices,” *Adv. Sci.* **7**(14), 2000799 (2020).
47. T. Cui, B. Bai, and H. B. Sun, “Tunable metasurfaces based on active materials,” *Adv. Funct. Mater.* **29**(10), 1806692 (2019).
48. S. Wang et al., “Nanoengineered spintronic-metasurface terahertz emitters enable beam steering and full polarization control,” *Nano Lett.* **22**(24), 10111–10119 (2022).
49. C. Liu et al., “Active spintronic-metasurface terahertz emitters with tunable chirality,” *Adv. Photonics* **3**(05), 056002 (2021).
50. S. Zhang et al., “Solitary beam propagation in periodic layered Kerr media enables high-efficiency pulse compression and mode self-cleaning,” *Light Sci. Appl.* **10**(1), 53 (2021).
51. K. Fan et al., “Phototunable dielectric Huygens’ metasurfaces,” *Adv. Mater.* **30**(22), 1800278 (2018).
52. I. Al-Naib et al., “Effect of local field enhancement on the non-linear terahertz response of a silicon-based metamaterial,” *Phys. Rev. B* **88**(19), 195203 (2013).
53. D. Riffe, “Temperature dependence of silicon carrier effective masses with application to femtosecond reflectivity measurements,” *J. Opt. Soc. Am. B* **19**(5), 1092–1100 (2002).
54. K. Sokolowski-Tinten and D. von der Linde, “Generation of dense electron-hole plasmas in silicon,” *Phys. Rev. B* **61**(4), 2643–2650 (2000).
55. D. Aspnes and A. Studna, “Dielectric functions and optical parameters of Si, Ge, GaP, GaAs, GaSb, InP, InAs, and InSb from 1.5 to 6.0 eV,” *Phys. Rev. B* **27**(2), 985–1009 (1983).
56. P. Lalanne et al., “Light interaction with photonic and plasmonic resonances,” *Laser Photonics Rev.* **12**(5), 1700113 (2018).
57. J. Yang, H. Giessen, and P. Lalanne, “Simple analytical expression for the peak-frequency shifts of plasmonic resonances for sensing,” *Nano Lett.* **15**(5), 3439–3444 (2015).
58. W. Yan, P. Lalanne, and M. Qiu, “Shape deformation of nanoresonator: a quasinormal-mode perturbation theory,” *Phys. Rev. Lett.* **125**(1), 013901 (2020).
59. A. Kumar et al., “Color-sensitive ultrafast optical modulation and switching of terahertz plasmonic devices,” *Adv. Opt. Mater.* **6**(15), 1800030 (2018).
60. K. Papatryfonos et al., “Refractive indices of MBE-grown $\text{Al}_x\text{Ga}_{(1-x)}\text{As}$ ternary alloys in the transparent wavelength region,” *AIP Adv.* **11**(2), 025327 (2021).
61. S. Logothetidis et al., “Optical properties and temperature dependence of the interband transitions of cubic and hexagonal GaN,” *Phys. Rev. B* **50**(24), 18017–18029 (1994).
62. L. Cong et al., “Temporal loss boundary engineered photonic cavity,” *Nat. Commun.* **12**(1), 6940 (2021).

Haoyang Zhou received his BS degree from the School of Physics, China University of Mining and Technology, in 2017. He is currently pursuing his PhD at the Department of Physics, Fudan University. His research interest focuses on dynamic metamaterials/metasurfaces.

Sheng Zhang received his BS degree from the Department of Physical Science and Technology, Wuhan University, in 2018. Currently, he is pursuing his PhD at the Department of Physics, Fudan University. His research interests include spintronics terahertz emitters and ultrafast optics.

Shunjia Wang received his BS degree from the Department of Physics, Fudan University, in 2019. Currently, he is pursuing his PhD at the Department of Physics, Fudan University. His research interests include spintronics terahertz emitters and terahertz metasurfaces.

Zhensheng Tao is a professor of the Department of Physics at Fudan University since 2018. His research activity is devoted to experimental research in optics and condensed matter physics, with particular interest in ultrafast nonequilibrium light–matter interaction and the development of ultrafast technologies.

Qiong He is a professor of the Department of Physics at Fudan University. His research activity is devoted to experimental research in

nanophotonics and metamaterials. He was awarded as Highly Cited Researcher 2022 (Clarivate).

Lei Zhou is a “Xi-De” chair professor and dean of the Department of Physics at Fudan University. He works in the field of nanophotonics and metamaterials, was elected as an OSA Fellow in 2019 and

won the second prize of National Natural Science of China in 2019. He was awarded as Highly Cited Researcher 2019 (Clarivate). He is the co-editor-in-chief of *Photonics Insights*, and the managing editor of *Nanophotonics*.

Biographies of the other authors are not available.